Supplementary Information for

Novel fractional crystallization route to porous TiO_2-Fe_2O_3 composites: large scale preparation and high performances as photocatalyst and Li-ion battery anode

Li Li, Zhang Jianbo, Zhu Qingshan*

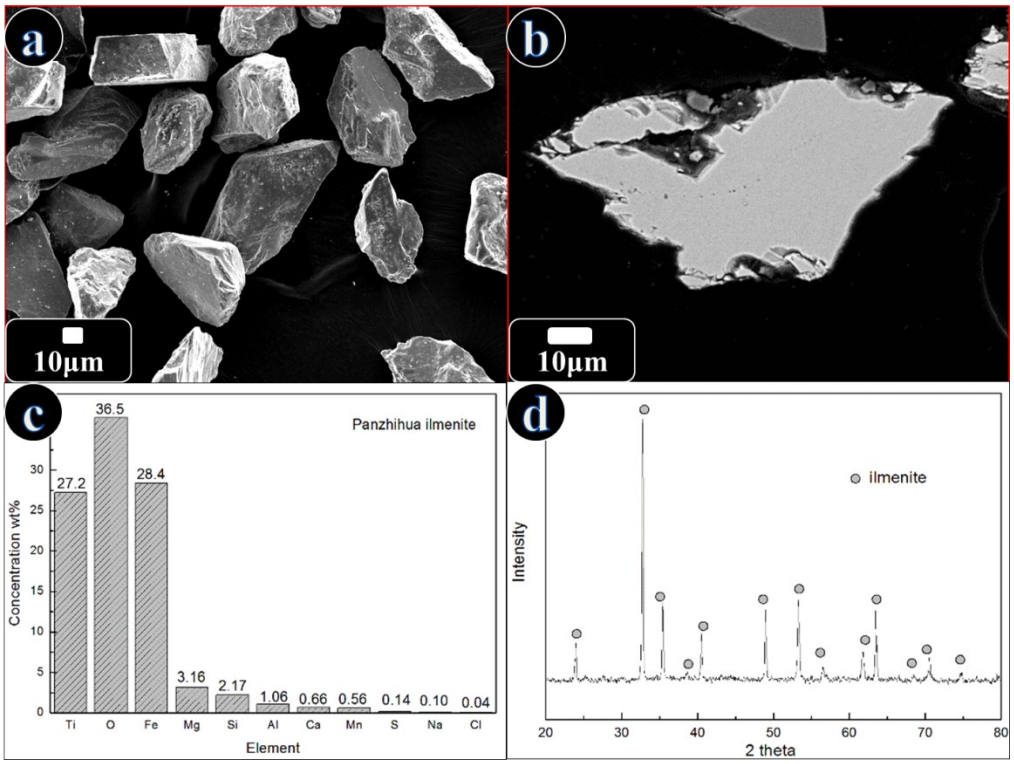

Fig. S1 Integrated characterizations of the Panzhihua ilmenite particles. SEM images of (a) overview of the pristine ilmenite particles, (b) the cross-section of a single particle, (c) XRF bar chart of the ilmenite, (d) XRD spectra of the ilmenite particles.

The morphology and constituent of Panzhihua ilmenite has been investigation by SEM, XRD and XRF. A panoramic view of the ilmenite particles reveals that the pristine ilmenite particles (obtained via a stepwise grinding-sieving treatment) used as the starting material for the formation of porous TiO_2-Fe_2O_3 composite particles possess irregular shape with an average center diameter of 50-75μm (Fig. S1a).The close observation of the cross section of an ilmenite particle indicates the uniform and compact nature of its inner section (Fig. S1b). The XRD spectra shown in Fig. S1 c exhibit the existence of a single ilmenite phase. XRF analysis confirms that, except for Ti, Fe and O (as the target elements), Mg, Ca, Al, and Si are the primary impurities. Most of those impurities may exist as part of a solid solution because they can notbe observed in the XRD pattern.

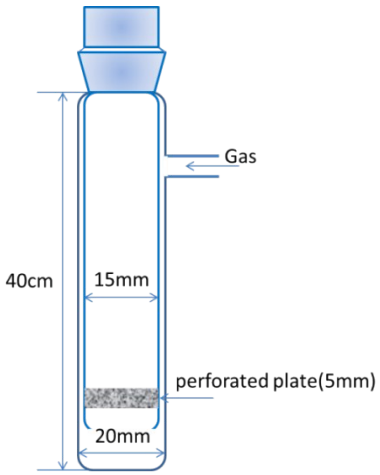

Fig. S2 Schematic of the fluidized bed reactor.

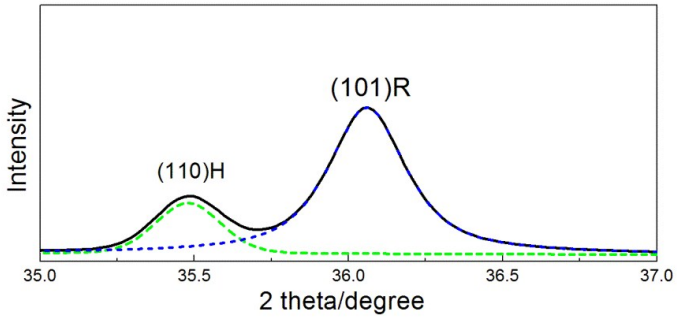

Fig. S3 Deconvolution of XRD patterns of sample S1 in Table 1.

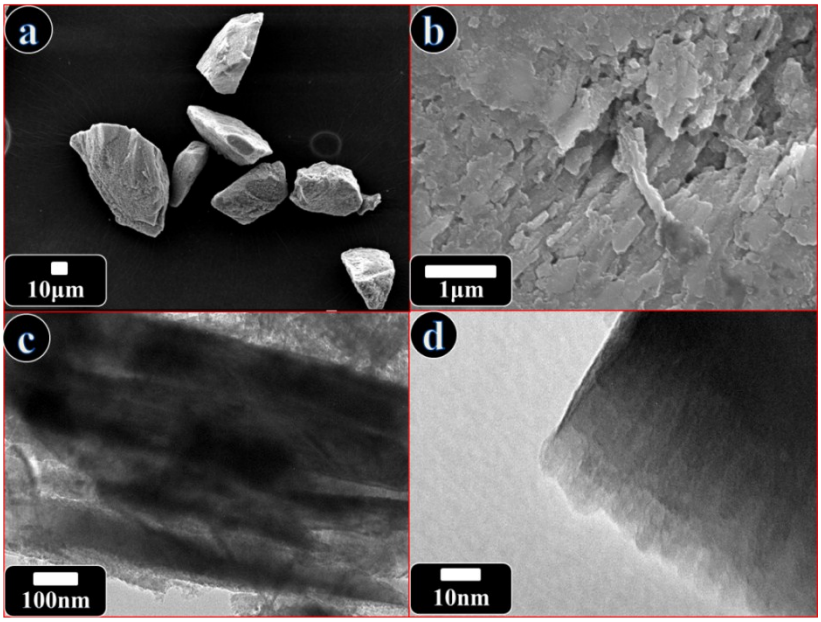

Fig. S4 SEM (a-b) and TEM (c-d) images of the porous particles (sample S2) at different magnifications.

Fig. S4a exhibits that the final porous TiO_2-Fe_2O_3 products possesses similar size to that of the staring raw materials. A magnified view of the product particle surface shows that these particles are assembled by laminary TiO_2 crystals (Fig. S4b), which can be further confirmed by TEM characterization (Fig. S4c). Moreover, from Fig. S4c, a mesoporous structure with 10-50nm in pore diameter can be seen clearly. A close TEM observation (Fig. S4d) on the edge of the laminary structure indicates the existence of micropores with 1-2nm in diameter, which may be attributed to the corrosion of TiO frame in the acid leaching process.

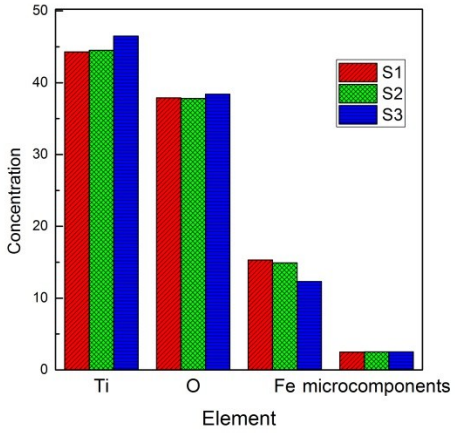

Fig. S5 XRF bar chart of the as obtained samples in Table 1

Table S1 XRF Chemical Compositions of the raw material (ilmenite) and the asobtained samples in Table 1.

Samples	**Ti**	**Fe**	**O**	**Trace elements**					
				Mg	Si	Mn	Al	Ca	Na
Panzhihua ilmenite	27.2	36.5	28.4	3.16	2.17	0.56	1.06	0.66	0.10
S1	44.3	15.3	37.9	1.24	0.47	0.40	0.12	0.10	0.03
S2	44.5	14.9	37.8	1.22	0.53	0.39	0.15	0.11	0.03
S3	46.5	12.3	38.4	1.21	0.56	0.38	0.13	0.10	0.02

The XRF results show that the Fe content in the products decreases with the elongated reduction duration, indicating that the extension of the reduction time favors the acid leaching of Fe (Fig. S5, Table S1). It can also be seen form Table S1 that, although natural ilmenite is used as the starting material, the impurity contents in the final products are on a low level (below 3%). Moreover, both the total contents of all impurities and the respective contents of various trace elements are almost on the same level in different samples.

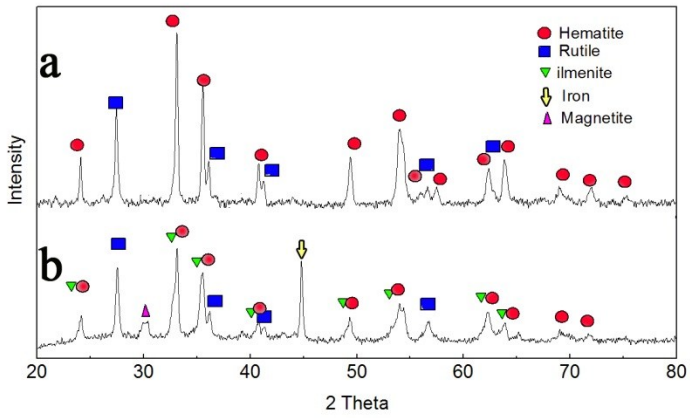

Fig. S6 XRD patterns of the samples obtained after oxidization at 800℃ for 40min(a), and reduction at 600℃ of the oxidized particles(b).

Fig. S6a shows the X-ray diffraction (XRD) pattern of the ilmenite oxidized at 800℃ for 40min. The main crystal phases of the product are TiO_2(rutile) and Fe_2O_3(Hematite), indicating the oxidation of ilmenite. Fig. S6b is the XRD pattern of the particles after a subsequent reduction treatment, which exhibits that the diffraction peaks indexed to hematite phase get broader and a slight move towards lower angle region is observed. Together with the decreased diffraction intensity of the peaks of the rutile, it can be concluded that the recombination reaction occurs and little amount of ilmenite is formed in addition to Fe and Fe_3O_4 (formed by entire and partial reduction of hematite, respectively).

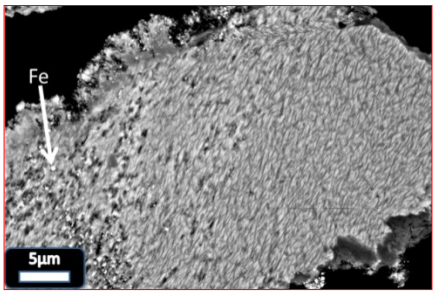

Fig. S7 Low-magnification back-scattered electron images of the cross-section for ilmenite oxidized at 800℃ for 40min and then reduced at 600℃ for 15min.

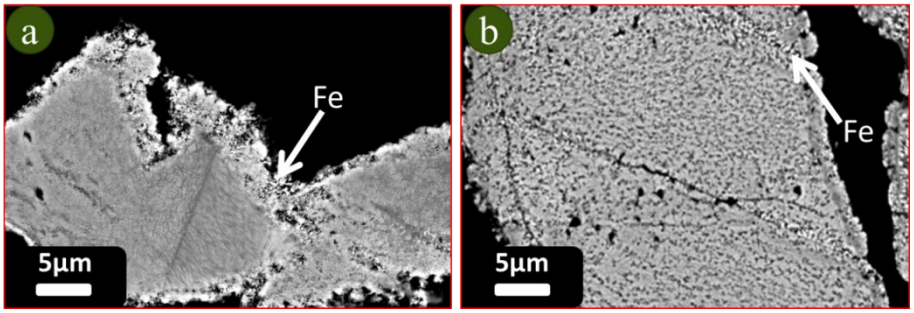

Fig. S8 Low-magnification back-scattered electron images of the cross-section for ilmenite oxidized at 800℃ for 40min and then reduced at 600℃ for (a) 5min, (b)30min.

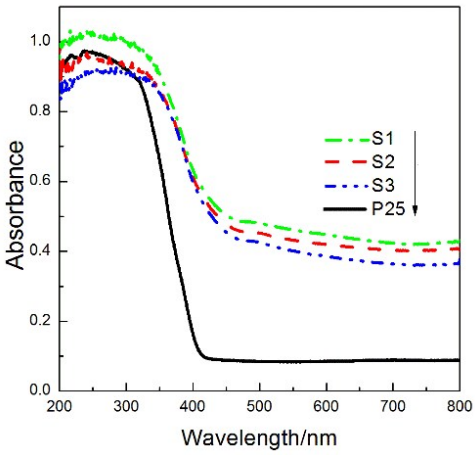

Fig. S9 UV–vis diffusive reflectance spectra of the samples in Table 1.

The heterostructure of Fe_2O_3-TiO_2 brings a wider range of light absorption. Fig. S9 shows the UV−visible diffuse reflectance spectra (DRS) of the samples. Apparently, the loading of metal oxides remarkably promotes the light harvesting ability and further extended the absorption range, as compared with P25.The relative band gap energy of the catalyst decreased in the order: P25(3.02eV)>S3>S2>S1 (Table S2). From the above discussion, it could be seen clearly that S2 had the proper absorption at the visible region and the band gap energy (1.65 eV), which was the prerequisite of a good photocatalyst under visible light.

Table S2 Optical band gap energy and XPS data of the catalysts

Sample	Optical band gap energy / eV	Atom ratio of O:Ti:Fe on the surface	Relative contents of the elements in the				
			Ti		O		
			Ti^{4+}	Ti^{3+}	$O_{lattice}$	$OH_{surface}$	$O_{abs.}$
S1	1.61	100:31.5:3.6	96.72	3.28	75.95	23.41	0.64
S2	1.65	100:31.6:3.5	98.16	1.84	76.12	23.84	0.04
S3	1.85	100:32.2:2.8	96.43	3.57	78.44	19.65	1.91

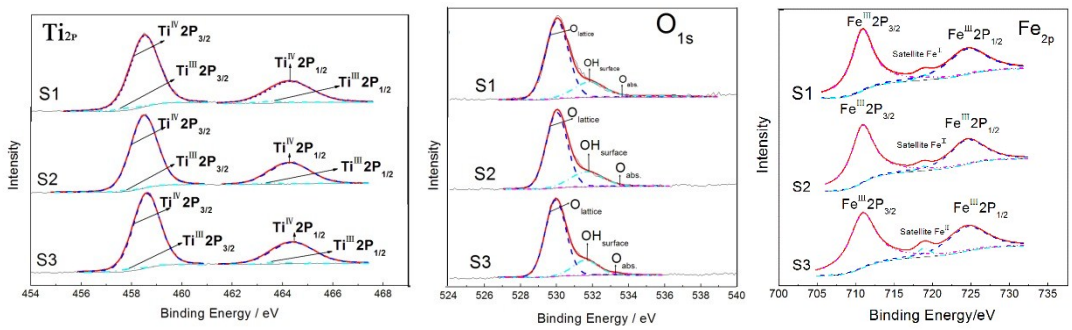

Fig. S10 X-ray photoelectron spectra (XPS) of the as-prepared product, and high-resolution XPS Ti2p, O1s and Fe2p spectrum.

The XPS spectra of the as-prepared product confirms the existence of Ti, O and Fe, and the minim impurities cannot be detected because of their tiny little amount. The Fe content in the surface section (as can be detected by XPS, see Table S2) is much lower than the total Fe content(Table S1), for the Fe near the surface section is eliminated in the acid leaching treatment, and most of the Fe_2O_3 phase concentrates on the central part.

Fig. S10-Ti2p shows the XPS spectra of the Ti2p region. The binding energy at 458.8 and 464.6 eV can be attributed to the $Ti_{2p3/2}$ and $Ti_{2p1/2}$ core levels of the as-prepared samples, respectively[1]. There is no apparent difference in the Ti_{2p} peak position for all the samples. The chemical states of titanium (Ti^{4+} and Ti^{3+}) are analyzed in detail by deconvolution by using Gaussian mixture peak fitting.[2] As shown in Table S2, the Ti^{3+}content is much lower than that of Ti^{4+} in the surface region，indicating an oxygen-rich status. Especially, sample S2 has the lowest surface Ti^{3+} ratio, which may be one of the reasons for its high catalytic activity, for Ti^{3+} dose not favor the photocatalytic performance of titanium oxide[1].

Fig. S10-O1s shows the XPS spectra of the O1s region. Generally, the photoelectron peaks of O1s can be curve fitted at about 529.9, 531.9, and 533.4 eV, which correspond to the titania lattices, surface hydroxyl groups, and adsorbed oxygen mainly from adsorbed water molecules.[3-4] This Figure also illuminates that the quantity of the adsorbed oxygen on the surface of the samples could be neglected, and the surface hydroxyl groups are abundant, whose concentration follow the sequenceS2>S1>S3(Table S2). As has been previously reported[5], the increase of the surface hydroxyl would lead to the enhancement of the photocatalytic efficiency. Thus the increased percentage of surface hydroxyl on S2 will increase photocatalytic oxidation property

All the peaks in the high-resolution XPS Fe_{2p} spectrum(Fig. S10-Fe2p) can be indexed to Fe^{3+}($Fe_{2p3/2}$: 710.9eV，$Fe_{2p1/2}$: 724.5eV, Fe^{3+} satellite: 718.8eV)[6], no Fe^{2+} characteristic peak can be found, from which an oxidized status can be confirmed on the surface region. Fe element is in the highest oxidation state.

From the above mentioned XPS results, it can be seen that S2 possesses the lowest Ti^{3+}content and the highest hydroxyl content, both of which favors the improvement of the photocatalytic performance. This can partly explain the best photocatalytic performance of S2.

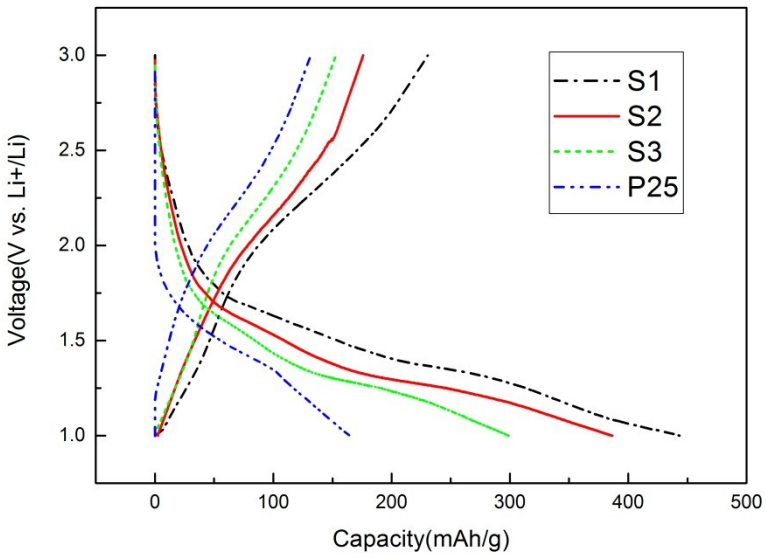

Fig. S11 The first discharge–charge cycling plots of P25 and the different TiO_2-Fe_2O_3 composites samples in Table 1, cycled in the voltage range of 1.0-3.0V at a current density of 0.2mA*cm^{-2}.

Table S3 discharge capacities and Coulombic efficiencies of the Samples in Table 1

Samples	1st discharge capacities/ mAh*g-1	1st Coulombic efficiencies	2nd discharge capacities/ mAh*g-1	2nd Coulombic efficiencies	3rd Coulombic efficiencies	4th Coulombic efficiencies	100th discharge capacities/ mAh*g-1	100th Coulombic efficiencies
S1	443.2	52.2%	261.9	90.1%	92.1%	95.2%	198.2	98.7%
S2	382.5	46.1%	198.2	89.4%	95.0%	98.1%	183.9	99.6%
S3	298.9	51.3%	173.0	89.3%	94.6%	97.1%	148.1	98.6%
P25	163.4	80.7%	155.6	95.0%	99.7%	99.8%	109.6	98.9%

Reference

[1] Chen, X. B.; Lou, Y. B.; Samia, A.; Burda, C.; Gole, J. L. Formation of Oxynitride as the Photocatalytic Enhancing Site in Nitrogen-Doped Titania Nanocatalysts: Comparison to a Commercial Nanopowder, *Adv. Funct. Mater.* **2005**, *15*, 41-49.

[2] Yu, J. G.; Zhao, X. J.; Zhao, Q. N.; Du, J. C. XPS Study on TiO_2 Photocatalytic Thin Film

Prepared by Sol-gel Method. *Chin. J. Mater. Res.* **2000,** *14*, 203-209.

[3] Li, G. Q.; Liu, C. Y.; Liu, Y. Different Effects of Cerium Ions Doping on Properties of Anatase and Rutile TiO_2. *Appl. Surf. Sci.* **2006**, *253*, 2481-2486.

[4] Liu, Z. L.; Guo, B.; Hong, L.; Jiang, H. X. Preparation and Characterization of Cerium Oxide Doped TiO_2 Nanoparticles. *J. Phys. Chem. Solids* **2005**, *66*, 161-167.

[5] Nakamura, R.; Nakato, Y. In situ FTIR studies of primary intermediates of photocatalytic reactions on nanocrystalline TiO2 films in contact with aqueous solutions. *J. Am. Chem. Soc.* **2004**, *126*, 1290-1298.

[6] Qin, L.; Pan, X.; Wang, L.; Sun, X.; Zhang, G.; Guo, X. Facile Preparation of Mesoporous TiO_2(B) Nanowires with Well-dispersed Fe_2O_3 Nanoparticles and Their Photochemical Catalytic Behavior. *Applied Catal. B: Environ.* **2014**, *150-151*, 544-553.